Energy Conversion and Management 315 (2024) 118809

Contents lists available at ScienceDirect

Energy Conversion and Management

journal homepage: www.elsevier.com/locate/enconman

Extreme heat flux cooling from functional copper inverse opal-coated manifold microchannels

Daeyoung Kong [b,a], Heungdong Kwon [a], Bongho Jang [c], Hyuk-Jun Kwon [c], Mehdi Asheghi [a], Kenneth E. Goodson [a], Hyoungsoon Lee [b,*]

[a] *Department of Mechanical Engineering, Stanford University, Stanford CA 94305, USA*
[b] *School of Mechanical Engineering, Chung-Ang University, Seoul, 06974, South Korea*
[c] *Department of Electrical Engineering and Computer Science, Daegu Gyeongbuk Institute of Science and Technology (DGIST), Daegu 42988, South Korea*

A R T I C L E I N F O

Keywords:
Thermal management
Single- and two-phase cooling
Manifold microchannel
Copper inverse opals

A B S T R A C T

The utilization of a hierarchical microstructure and three-dimensional (3D) manifold for liquid delivery and liquid/vapor extraction could potentially improve the single-phase/two-phase thermal performance of micro-coolers for high-heat-flux microelectronics applications exceeding 1 kW cm^{-2}. In this work, we utilize a conformal coating of 8-μm-thick copper inverse opal (CuIO) films with ~ 5-μm pore size on silicon microchannels in combination with a polydimethylsiloxane 3D manifold to remove heat fluxes up to 1147 W cm^{-2} under a water inlet temperature and flow rate of 20 °C and 200 g min^{-1}, respectively. We achieved a convective thermal resistance of 0.068 cm^2 K W^{-1} and total pressure drop of 32 kPa. Moreover, owing to copper micropores, a better hot-spot temperature uniformity (<6 K) with the aid of improved boiling nucleation was achieved. The interchip microchannel with a functional porous material and 3D manifold offers a disruptive thermal-management solution for high-performance electronic devices such as data centers, defense weapons, and power electronics for electric vehicles.

1. Introduction

The exponential demand for high-performance electronics in data centers, defense weapons, nuclear fusion reactors, and power electronics has resulted in an increase in both total power and heat flux (heat dissipation per unit area) in electronic devices [1]. AlGaN/GaN high-electron-mobility transistors [2] have a high breakdown voltage, operating frequency, and high output power, resulting in chip-level heat fluxes [3] exceeding 1 kW cm^{-2}. Employing conventional indirect cooling to manage ultrahigh heat fluxes exceeding 1 kW cm^{-2} is challenging because of package-level issues, including a parasitic temperature rise due to thermal interface materials, as well as system-level limitations such as an operatable junction temperature and high flow-rate requirements, which cause a significant pressure drop [4,5]. To address this problem, the embedded (direct) microchannel cooling of microelectronics was first introduced in the early 1980 s by Tuckerman and Pease [6], followed by a series of cooling strategies using microstructure [7–11], jet impingement [12–14], spray cooling [15,16], surface modification [17,18], and nanofluids [19–21]. All these approaches yield increased heat transfer coefficients and critical heat fluxes [22,23]; however, they require a large pumping power, have diminished reliability, and increase microfabrication and packaging integration complexities.

A three-dimensional (3D) manifold microchannel (MMC) technology is introduced to shorten the flow path in the narrow embedded microchannels by distributing/extracting the cold/warm fluid using 3D-manifold conduit branches, resulting in a significantly low pressure drop and pumping power [24,25]. Because the cold fluid is distributed uniformly by the 3D manifold and delivered perpendicular (impinging jet-like) to the heated microchannels, both the magnitude and nonuniformity of the hot spots are significantly reduced [26–28]. Wang and Ding [29] fabricated a heat spreader by etching a manifold and microchannels with $W_{ch} = 100$ μm and $H_{ch} = 20$ μm using a silicon wafer as a substrate and experimentally demonstrated a uniform temperature distribution using deionized (DI) water. They achieved a thermal resistance of 1.83 K W^{-1} with a low flow rate of 6.79 mL min^{-1} and a maximum heat flux of 18.9 W cm^{-2} in a heating area of 19.4 × 9.1 mm^2. Escher et al. [30] fabricated a compact MMC by microfabrication using a silicon substrate and conducted parametric studies on the manifold and microchannel

* Corresponding author.
E-mail address: leeh@cau.ac.kr (H. Lee).

https://doi.org/10.1016/j.enconman.2024.118809
Received 25 May 2024; Received in revised form 10 July 2024; Accepted 13 July 2024
Available online 20 July 2024

Nomenclature

A	area [m^2]
AR	aspect ratio
d_p	diameter of pore [m]
d_n	diameter of neck [m]
f	friction factor
G	mass flux [kg/s-m^2]
H	height [m]
HTC	heat transfer coefficient [W/m^2-K]
k	thermal conductivity [W/m-K]
L	total chip length [m^2]
m	fin constant
N_{ch}	number of channels
Nu	Nusselt number
ΔP	pressure drop [Pa]
q''	heat flux [W/m^2]
R	thermal resistance [m^2-K/W]
Re	Reynolds number
r	radius of pore [m]
T	temperature [K]
T_f	mean fluid temperature [K]
T_h	mean heater temperature [K]
W	width [m]

Greek symbols

δ	thickness [m]
η_f	fin efficiency
θ	angle [degree]

Subscripts

avg	average
b	base
bot	bottom
CuIO	copper inverse opal
ch	channel
cond	conduction
conv	convection
eff	effective
fin	fin
h	heater
in	inlet
junc	junction
MF	manifold
out	outlet
si	silicon substrate
sat	saturation
sub	subcooled
top	top
tot	total

geometries and operating conditions. The use of tapered inlet and outlet ensured constant pressure gradients across the microchannel inside their heatsink, resulting in a uniform fluid distribution. With an optimal MMC design, a heat flux of 700 W cm^{-2} corresponding to a thermal resistance of 0.023 K W^{-1} was removed at a flow rate of 1.3 L min^{-1} using water as a working fluid in a footprint area of 20 × 20 mm^2 while obtaining a pressure drop of 22 kPa. Jung et al. [31] fabricated an embedded manifold microchannel on a silicon substrate and demonstrated its thermal and hydraulic performance using single-phase water cooling. They used tapered entries to mitigate the pressure drop induced by sudden contractions at the plenum entrance, resulting in a 60 % reduction in pressure drop to around 2.6 kPa at a flow rate of 0.1 L min^{-1} and heat flux dissipation of 250 W cm^{-2}. In addition, the numerical study revealed that it is possible to remove 850 W cm^{-2} of heat flux at the same flow rate. van Erp et al. [32] monolithically fabricated microchannels and manifolds on a single silicon substrate as an embedded cooling module using microfabrication. An analog-to-digital converter was fabricated using GaN in a footprint area of around 2.8 × 2.8 cm^2, and approximately 1700 W cm^{-2} was dissipated at a flow rate of 0.06 L min^{-1}, resulting in a pressure drop of 125 kPa. They experimentally demonstrated that the electrical–thermal co-design could achieve a cooling effect that exceeded a heat flux of 1 kW cm^{-2}. In addition to water, two refrigerants, namely, HFE-7100 [33–35] and R-245fa [36], which have the advantage of being dielectric liquids, dissipated a heat flux of 900 and 500 W cm^{-2}, respectively, with flow boiling on a Si-based MMC. However, the poor thermophysical characteristics of these dielectric liquids compared to water cause the junction temperature to increase rapidly in response to a small heat flux. In addition, the large pressure drop caused by the flow boiling, which compensates for the removal of the high heat flux, could result in the requirement of an extremely high pumping power.

There have been a few attempts to integrate porous media into the manifold microcooler. Wang et al. [37] inserted silicon nanowires into the microchannel and fabricated a silicon-based MMC. Using DI water, they observed the enhanced heat transfer and mitigation of flow instability during two-phase flow, achieving a heat flux of 431 W cm^{-2} at a maximum mass flux of 1250 kg m^{-2} s^{-1}. Kim et al. [38] fabricated copper inverse opals on a smooth Si substrate and integrated a silicone rubber-based manifold. They used DI water as a working fluid and achieved a critical heat flux of 323 W cm^{-2} at a mass flux of 472 kg m^{-2} s^{-1}. They found that temperature nonuniformity could be alleviated by flow boiling while keeping the pressure drop low to under 0.6 kPa. Sun and Li [39] prepared an MMC using a sintered copper with 1-μm copper powder to promote flow boiling. They removed the heat flux up to 360 W cm^{-2} over a heating area of 5 cm^2 using three different working fluids: DI water, HFE-7100, and HFE-7100/water mixture. They demonstrated that the MMC with a fully porous coating exhibited superior heat transfer performance than locally covered MMC. Although several researchers have explored the thermofluidic characteristics of embedded MMCs, a comprehensive insight into the microfluidic behavior, the effect of combination with porous metals, and constraints for optimizing the thermofluidic performance of MMC have not been provided in detail.

In this study, extreme cooling is achieved using interchip cooling with a manifold microchannel structure coated with a conformal microporous structure. We fabricate silicon microchannels (*width* = 50, 100, and 200 μm and *height* = 100 μm) that are conformally coated with electroplated copper inverse opals (CuIOs) to achieve improved performance. In addition, we utilize a polydimethylsiloxane (PDMS) 3D manifold cover with a channel height of 900 μm and inlet and outlet channel widths of 700 and 1400 μm, respectively, to reduce pressure drop and increase flow uniformity across the chip. We demonstrate chip temperature and pressure drop by thermal-fluid tests for the characterization in terms of operating conditions and geometries and further evaluate the thermal performance of the cooling scheme.

2. Experimental method

2.1. Copper inverse opal structure on a microchannel heat sink

The microchannel with the porous metallic structure was fabricated on a 6-inch silicon wafer as shown in Fig. 1. Microchannels with a depth of 100 μm were fabricated on the wafer via a deep reactive-ion etching (DRIE) process. Then, a working electrode pad to electrodeposit a

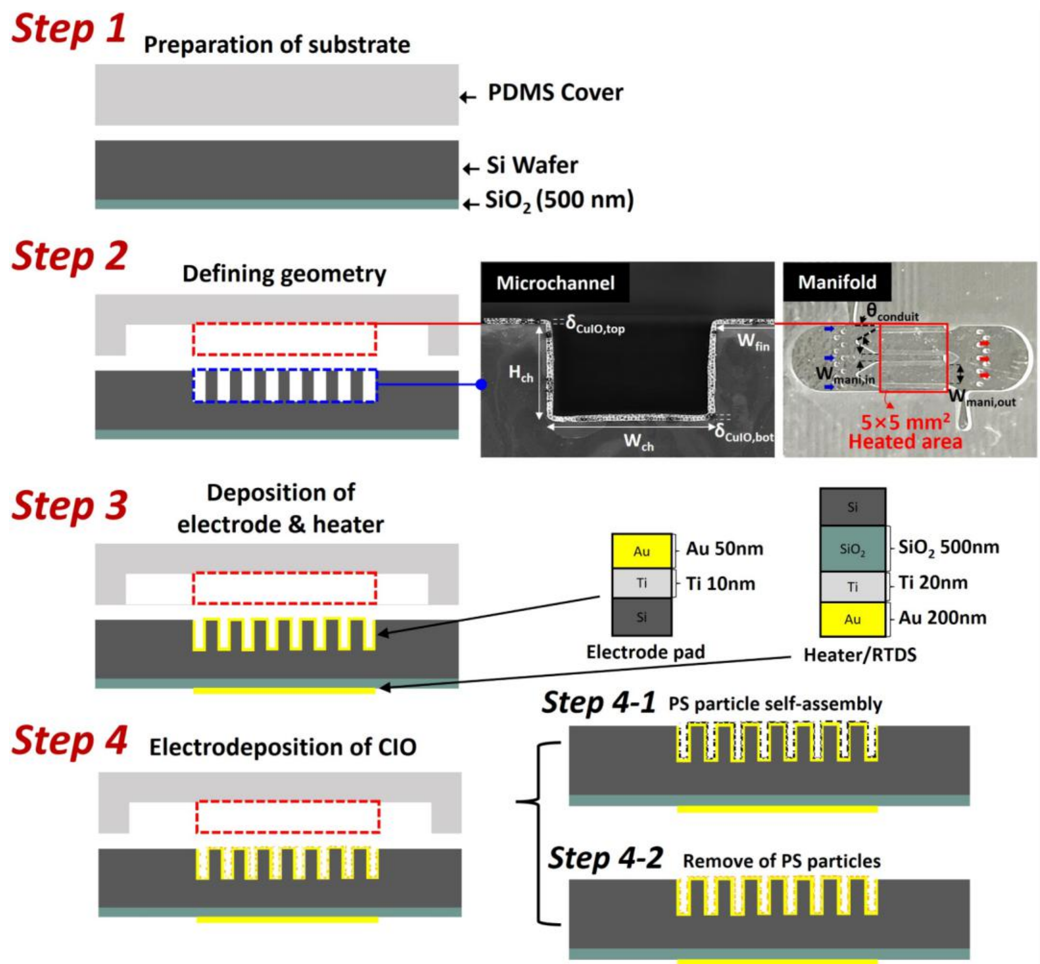

Fig. 1. Fabrication step of CuIO built-in MMC cooler. Step 1: Preparation of silicon wafer and PDMS. Step 2: Fabrication of silicon microchannel and PDMS manifold using DRIE and PDMS replica from a mold, respectively. Step 3: Metal deposition on a Si substrate. A Ti/Au layer is deposited on the microchannels owing to the post-electrodeposition. On the backside of the microchannel, a thin-film heater is deposited for thermal testing. Step 4: Self-assembly of PS spheres and electrodeposition for creating the CuIO structure. Step 5: Test module assembly for a thermal fluid test.

porous metallic structure and a heater for thermal test on the opposite side of the wafer was deposited for Ti/Au layers of 20 nm/100 nm and 20 nm/200 nm in an area of 5×5 mm^2, respectively. The gold electrode pad for the electrodeposition was immersed in 1-mM aqueous sodium 3-mercapto-1-propanesulfonate solution for at least 24 h to convert it to a hydrophilic surface. A solution of 30 μl of 5 % wt/vol polystyrene (PS) spheres ($d_p = 5$ μm) was dispersed using a drop-casting method on the gold electrode cleaned with DI water. Dispersed polystyrene spheres were self-assembled into a sacrificial polycrystalline packing template using sedimentation while the substrate was heated to ~ 60 °C on a hot plate to quickly evaporate the solvent (water in this study) and reduce the coffee ring effect. The dried PS template was sintered for 80 min at 100 ± 2 °C in a vacuum oven by monitoring the temperature of the supporting plate using a thermocouple. The sintered PS template was immersed in an aqueous electrolyte solution (0.5-M $CuSO_4$ + 0.2-M H_2SO_4) and electrodeposited with copper in the space inside the template using a potentiostat (Bio-Logic SP300). The three-electrode cell comprised a working electrode connected to the sintered template, a counter electrode connected to an oxygen-free copper block, and an Ag/AgCl reference electrode. Because of the hydrophobic nature of the PS template, 4 μl of ethanol was dropped on the PS template to promote wicking of the electrolyte to the gold surface before electrodeposition. Electrodeposition was conducted for 90 min at a constant current density of 2.5 mA cm^{-2} to obtain a uniform porous copper structure of 1–2 layers. Finally, the PS spheres were dissolved in tetrahydrofuran, an organic solvent, for at least 24 h to obtain a CuIO structure on the microchannel.

The detailed design and SEM images of the fabricated CuIOs on the microchannel are shown in Fig. 2. CuIOs can further promote nucleation boiling and increase critical heat flux (CHF) by increasing the capillary wicking to maintain a thin liquid film at the boiling surfaces [40]. However, the study of two-phase boiling is beyond the main scope of this paper.

One of the CuIO's characteristics, the permeability, is determined by the diameter of the necks between the inverse opals, which in turn depends on the sintering time of the polystyrene sacrificial spheres [41]: the longer the sintering time, the larger the neck size. The distribution of the characterized neck size with sintering time is shown in Fig. S1. In this study, we considered a sintering time of 80 min, which yielded an average neck size of ~ 1.5 μm to maximize the permeability of the fluid flowing into the CuIOs. In addition, the thickness of the CuIOs varies from the bottom (δ_{CuIO}=1.4 μm) to the top (δ_{CuIO}=6–8 μm) of the microchannels because of the nonuniformity of the electric field during the electrodeposition process [42]. The thickness uniformity of the CuIOs increased for wider microchannels (Fig. 2(e)–(j)) as the aspect ratio (AR=W_{ch}/H_{ch}) was increased from ½ to 2. The summarized dimensions for CIO-covered microchannel can be found in Table 1.

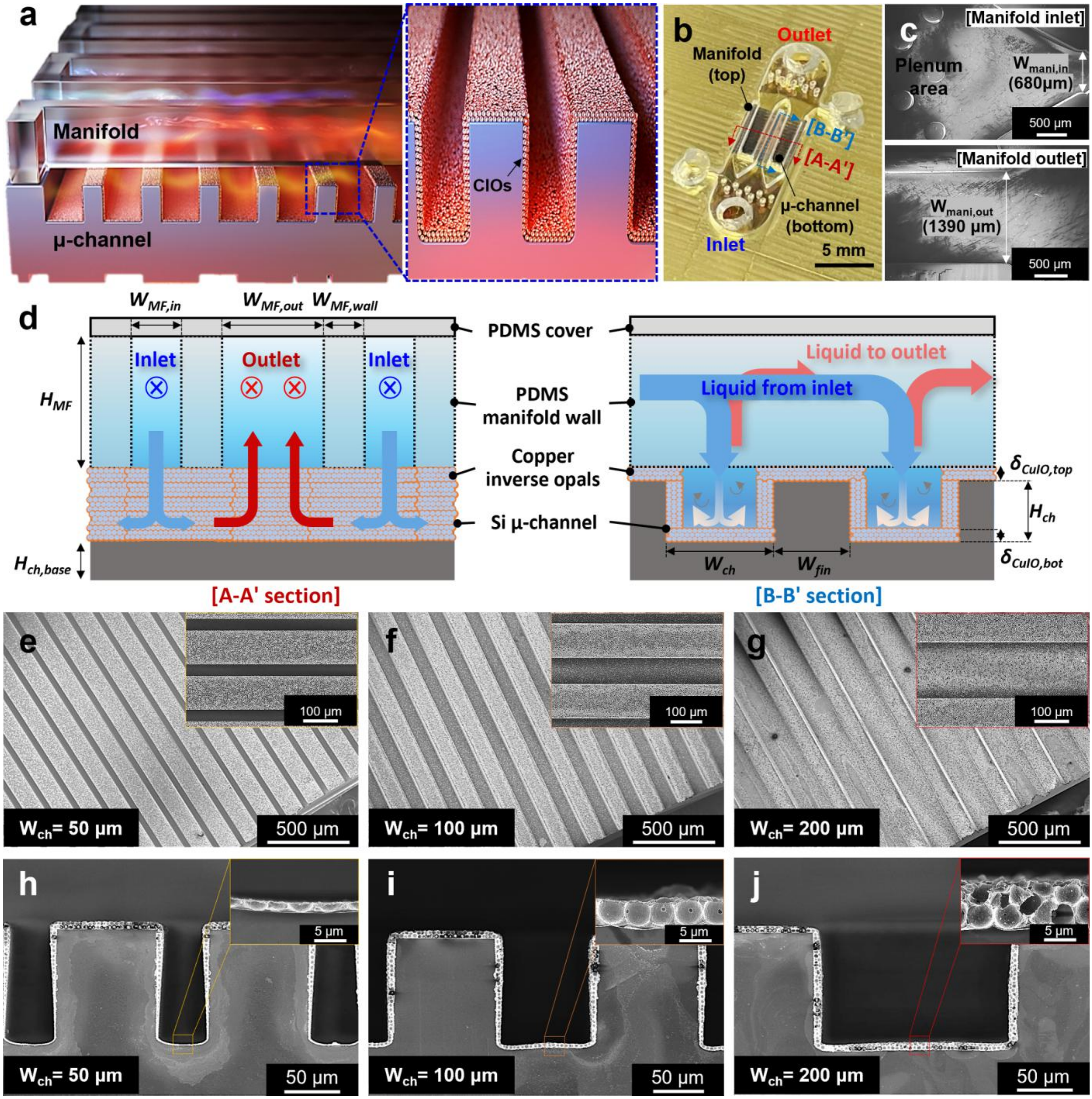

Fig. 2. Fabrication of the CuIO-coated MMC. (a) Graphical image of CuIO-MMC cooler. (b) Test device integrating a silicon microchannel with CuIOs and a PDMS manifold liquid-routing cover with a footprint area of 5×5 mm^2. (c) Scanning electron microscopy (SEM) images of the manifold inlet and an outlet section. The manifold has a 2-fold outlet/inlet width ratio. (d) Schematic illustration of the CuIO-MMC cooler. (e)–(g) Top-view and (h)–(j) side-view SEM images of a CuIO-grown microchannel with different channel widths (50, 100, and 200 μm). CuIOs are conformally fabricated with a certain thickness on the microchannel.

Table 1
Dimensions of the MMC cooler and the functional CuIOs.

Substrate	Sample index	H_{ch} [μm]	W_{ch} [μm]	W_{fin} [μm]	AR	N_{ch}	$\delta_{CuIO,top}$ [μm]	$\delta_{CuIO,bot}$ [μm]
CuIO-microchannel	A	119	53	99	2.2	33	8.2	1.6
	B	110	103	100	1.1	25	8.7	4.3
	C	116	206	101	0.6	16	6.7	6.7
Substrate	**Sample**	$\boldsymbol{H_{MF}}$ **[μm]**	$\boldsymbol{W_{MF,in}}$ **[μm]**	$\boldsymbol{W_{MF,out}}$ **[μm]**	$\boldsymbol{W_{MF,wall}}$ **[μm]**	$\boldsymbol{\theta_{conduit}}$ **[°]**		
Manifold	–	900	680	1380	300	30		

2.2. PDMS manifold cover and test module assembly

We utilized a PDMS manifold cover with a large height of 900 μm to reduce the pressure drop and flow nonuniformity across the chip. The manifold featured three inlet and two outlet conduits that were twice the width of the inlets. Specific information for the fabricated PDMS manifold can be found in Table 1. A mold for manufacturing the PDMS manifold was engraved on an acrylic plate with a depth of 900 μm using micro-CNC. A mixture of PDMS and a curing agent with a ratio of 1:8 was poured into the manifold mold and placed in a vacuum oven for 3 h to remove trapped air bubbles. Subsequently, the cured PDMS cover was removed from the mold, and holes were drilled in the in/out plenum and pressure ports so that the fluid could enter the inside of the cooler. The test module comprised a liquid route housing made of polycarbonate (PC), a PDMS cover, and a polyether ether ketone (PEEK) fixture to mount microchannel samples as shown in Fig. S2. Transparent PC and PDMS were selected to facilitate the high-speed visualization of bubbles. The PC housing consisted of an inlet and outlet, pressure port, and thermocouple insert as well. The PDMS cover had holes drilled in alignment with each port of the PC block so that the fluid moved into the manifold and microchannel without clogging. Here, silanol groups were introduced to each surface of silicon and PDMS by oxygen plasma treatment for the assembly of the CuIOs-MMC cooler. This enabled the formation of Si-O-Si bridges at the interface between two materials, creating a robust bond and preventing fluid leakage during flow tests [43]. PEEK compressed the microchannel sample, PDMS, and PC block to help prevent leakage at high system pressures and also served as an insulator during thermal tests. In addition, a hole as large as the heater size was drilled in the center so that the surface temperature could be measured by IR thermal imaging.

2.3. Test procedure and uncertainties

A system-level flow test loop for thermal and hydraulic experiments is depicted in Fig. 3. Once the test module was assembled, the module was mounted on the flow loop through the inlet and outlet fittings, the pressure inserts were connected to a differential pressure transducer (Omega PX409, ±0.25 %), and an absolute gauge pressure transducer (TRAFAG ECT8472, ±0.5 %) to set the outlet pressure to ∼ 1.2 bar. Further, the bulk fluid temperature in the inlet/outlet plenum was measured by inserting a K-type thermocouple (Omega KMQSS-062, ±1.1 °C). The working fluid was transported to the test section using a magnetically driven gear pump (Micropump GA-T23), and a Coriolis mass flow meter (KIF510, ±0.2 %) was installed behind the pump to measure the mass flow rate. A pre-heater (TECHNE TE-10D) was installed in front of the test module to set the desired inlet temperature, which was T_{in} = 25 °C in this study. Fifty-micrometer filters were placed in front of the pump and at both ends of the module to filter impurities that could accumulate in the pump and module. Black paint (ELE EP-10) with high emissivity was thinly coated on the heater to measure the surface temperature of the heater. The temperature distribution of the heated surface and the flow visualization was recorded using an IR camera (FLIR A655sc, ±2 °C) and a high-speed camera (FASTCAM Mini UX100), respectively. Once the heated fluid came out, it was cooled down by a plate heat exchanger connected to a liquid circulation chiller (Jeiotech HH20) and returned to the reservoir at ambient temperature.

Joule heating, which powers the metal serpentine heater, was computed by multiplying the voltage across the heater, V_{heater}, with the current flowing through the heater, I_{heater}. The heat flux was also determined as the applied heat divided by the heater area:

$$q''_{tot} = \frac{VI}{A_h} = \frac{q}{A_h} \tag{1}$$

The net heat transferred to the Si MMC was estimated by subtracting the parasitic conduction heat losses from the total heat, i.e., $q_{net} = q_{tot} - q_{loss}$. The heat loss was empirically obtained from the natural convection state considering the diffusion by the in-plane conduction of the silicon substrate and defined as the curve fitting $q_{loss} = -0.000123 \times (T_h - T_{in})^2 + 0.051 \times (T_h - T_{in}) + 0.0137$ [W], and the error for heat losses in the CIOs-MMC was 2.3 %–5.1 %.

The uncertainty of each instrument is given in Table 2. The accuracy of mass flow rate measurement at the inlet was 0.2 %. In addition, the

Table 2
Uncertainties of experimental apparatus and the results.

Component	Affected parameter	Uncertainty
Thermocouple (K-type)	$T_{f,in}$, $T_{f,out}$	±1.1 °C
Differential pressure transducer	ΔP_{tot}	±0.25 %
Absolute pressure transducer	P_{in}, P_{out}	±0.5 %
Coriolis mass flow meter	$\dot{m}$, G	±0.2 %
Power supply	q''	±0.2 %
Resistor	V_{heater}	±1 %
Shunt resistor	I_{heater}	±0.5 %
IR camera	T_h	±2 °C
Results	**Parameter**	**Maximum uncertainty**
Heat flux	q''_{heater}	±1.4 %
Total thermal resistance	R_{tot}	±14.0 %
Heat transfer coefficient	HTC, Nu	±16.0 %
Friction factor	f	±0.3 %

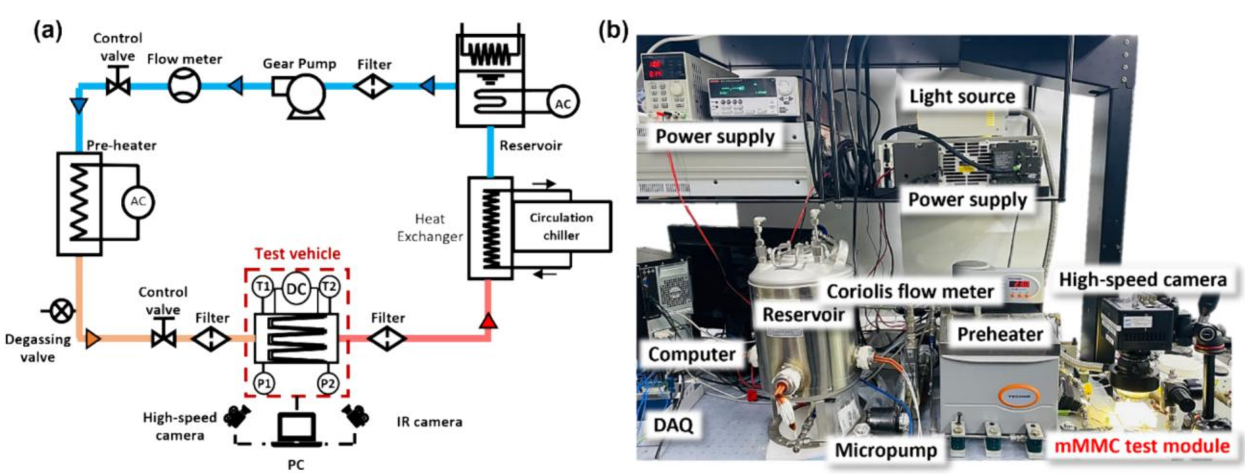

Fig. 3. Experimental setup for thermal–fluid performance evaluation. (a) Schematic of test flow loop facilities for thermohydraulic evaluation and (b) the corresponding image of flow loop components.

precisions of the resistors that received voltage and current through the voltage divider and shunt resistor were 1 % and 0.5 %, respectively. Thus, the uncertainty of q_{heater} was considered in Eq. (2) and calculated to be ± 1.4 %:

$$\left(\frac{U_{q_{heater}}}{VI}\right)^2 = \left(\frac{U_{V_{heater}}}{V_{heater}}\right)^2 + \left(\frac{U_{I_{heater}}}{I_{heater}}\right)^2 \tag{2}$$

The absolute gauge pressure and differential pressure transducer readings from inside the sample had precisions of 0.5 % and 0.25 %, respectively. The accuracy of the inlet and outlet thermocouples was ± 1.1 °C, and the temperature of the heated surface measured with the IR thermometer had an accuracy of ± 2 °C. The thermal resistance and heat transfer coefficient were correlated with the heat flux, heater temperature, and fluid temperature. Therefore, according to Eqs. (3) and (4), the total thermal resistance (R_{tot}) and heat transfer coefficient (h) in the MMC experiment exhibited uncertainties of 2.4 %–14.0 % and 2.7 %–16.0 %, respectively. It is noted that the Nusselt number (Nu) should have the same uncertainty level because it is propagated from the heat transfer coefficient.

$$\left(\frac{U_{R_{tot}}}{R_{tot}}\right)^2 = \left(\frac{U_{T_{heater,avg}}}{T_{heater,avg} - T_{f,in}}\right)^2 + \left(\frac{U_{T_{f,in}}}{T_{heater,avg} - T_{f,in}}\right)^2 + \left(\frac{U_{q''_{heater}}}{q''_{heater}}\right)^2 + \left(\frac{U_{q''_{loss}}}{q''_{loss}}\right)^2 \tag{3}$$

$$\left(\frac{U_h}{h}\right)^2 = \left(\frac{U_{T_{heater,avg}}}{T_{heater,avg} - T_{f,avg}}\right)^2 + \left(\frac{U_{T_{f,avg}}}{T_{heater,avg} - T_{f,avg}}\right)^2 + \left(\frac{U_{q''_{heater}}}{q''_{heater}}\right)^2 + \left(\frac{U_{q''_{loss}}}{q''_{loss}}\right)^2 \tag{4}$$

The friction factor (f) was correlated with the pressure drop and mass flow rate, which could be simply derived using Eq. (5) and showed an uncertainty of ± 0.3 %:

$$\left(\frac{U_f}{f}\right)^2 = \left(\frac{U_{\Delta P}}{\Delta P}\right)^2 + \left(\frac{U_{\dot{m}}}{\dot{m}}\right)^2 \tag{5}$$

3. Results and discussion

3.1. Effect of oxygen plasma treatment

Hydrophilic copper oxide surfaces are advantageous in terms of their potential uses, e.g., 1) the enhancement of heat-dissipation devices owing to their enhanced liquid replenishment, such as microfluidic cooling systems and heat pipes [44]; 2) the protection of Cu against further corrosion [45]. Therefore, we proceeded with oxygen plasma treatment (Femto Science, CIONE 6) to induce effective thermal diffusion by increasing wettability in porous media. Plasma treatment functionalizes porous copper as a hydrophilic surface under specific conditions (power of 100 W and frequency of 50 kHz under a base pressure of 0.1 torr for 1 min) after passing a constant flow of oxygen gas at 50 sccm [46]. By utilizing the plasma treatment, the contact angle (CA) of water on a surface can be altered from hydrophobic to hydrophilic owing to the increased surface energy of copper caused by oxygen plasma. To measure the wettability of the functionalized surface, the CA before/after oxygen plasma treatment was compared as shown in Fig. S3 (a) and (b). The CA before the treatment indicated a hydrophobic surface with an average of 90° through the entire channel width, while the surface after plasma treatment became substantially hydrophilic, with CA<50° [47]. In addition, the elemental composition of the two surfaces was analyzed by X-ray photoelectron spectroscopy (XPS), and the oxygen content was compared (Fig. S3(c)–(f)). In peak analysis, the two peaks of O1s showed lattice oxygen in CuO and –OH groups at binding energies of 530.8 and 531.9 eV, respectively. The proportion of total elemental oxygen increased from 29.8 % to 37.6 % on the surface subjected to oxygen plasma treatment, showing that the proportion of oxidized copper increased, and the surface became a hydrophilic surface [48].

3.2. Heat transfer and hydraulic performances

The thermal–hydraulic performance of the CuIOs-MMC was evaluated by employing DI water as a working fluid. Fig. 4(a) shows the behavior of the averaged junction temperature as the flow rates and applied heat fluxes are changed. The heat fluxes were intensified until the junction temperature reached $T_{junc} = 130$ °C. It is noted that the CuIOs on the three different microchannels was fabricated with different thicknesses and it was not possible to compare the geometric influence alone. The normalized area ratio of CuIOs in each microchannel was calculated as $A_{CuIO,Wch50}$: $A_{CuIO,Wch100}$: $A_{CuIO,Wch200}$ = 1:1.18:1.22. As expected, the junction temperature rose linearly with the heat flux and decreased as the flow rate increased. In addition, most of the two-phase boiling (red outline) as a subcooled bubbly flow was promoted at T_{junc} = 120 °C–130 °C with the aid of the micropores of CuIOs. The initial appearance of vapor bubbles marks a shift from a single-phase flow regime to a two-phase flow regime, accompanied by a significant change in heat transfer and pressure loss. Therefore, the onset of boiling (ONB) model capable of microchannel flow boiling was also implemented to predict the base temperature suitable for our CuIO-based microcooler [49]. The model includes the superheat temperature ($\Delta T_{sat} = T_{wall} - T_{sat}$), heat flux ($q''$), and contact angle ($\theta$). Using these inputs, the hydraulic–thermal inequality equation determines the necessary cavity radius for boiling incipience:

$$\{r_{\min}, r_{\max}\} = \frac{T_w + \frac{2\sigma C}{\rho_g h_{fg}}\frac{q''_{eff}}{k_f} - T_{sat}}{2\frac{q''_{eff}}{k_f}} \frac{\sin\theta}{1+\cos\theta}\left(1 \mp \sqrt{1 - \frac{4\frac{2\sigma C}{\rho_g h_{fg}}\frac{q''}{k_f}T_w}{\left(T_w + \frac{2\sigma C}{\rho_g h_{fg}}\frac{q''}{k_f} - T_{sat}\right)^2}}\right) \tag{6}$$

where r is the radius of the pore, and σ_f, ρ_f, k_f, and h_{fg} are the surface tension, density, thermal conductivity, and latent heat of DI water, respectively. C is the shape factor, C=1 + cosθ. To apply Eq. (6) to a microchannel with CuIOs, we estimated the superheat temperature that enables an ONB at the high heat flux of 500 and 1000 W cm^{-2} considering the neck size of the functionalized CIOs as illustrated in Fig. 4(b). Prior to plasma treatment ($\theta = 90°$), boiling ensued at relatively larger pore sizes with a rather low wall superheat. However, after plasma treatment ($\theta = 40°$), a much larger superheat of ΔT_{sat} = 22–32 K was required for boiling incipience owing to the highly wetting surface. Because the fabricated CuIOs had a pore size of d_p = ~5 μm and neck size of d_n = ~1.4 μm, the lowest superheat could be obtained, which matched well with the temperature results presented in Fig. 4(a).

The effective heat transfer coefficient is evaluated by averaging over the base area of the CuIOs-MMC while accounting for the fin efficiency, wetted area, and heat flux as follows:

$$h_{eff} = \frac{q'' A_h}{(T_b - T_f)\left[\left(A_{wet} - N_{ch}(2H_{ch} + W_{fin})L\right) + \left(N_{ch}\eta_{fin}A_{ch}\right)\right]} \tag{7}$$

where $T_b - T_f$ is the wall temperature difference from the base temperature and mean fluid temperature, and N_{ch} is the number of channels. The fin efficiency, η_{fin}, can be defined as $\eta_{fin} = \tanh(m_{fin}H_{ch}) / m_{fin}H_{ch}$, where $m_{fin} = (2h_{eff} / k_{si}W_{fin})^{1/2}$ and k_{si} is the thermal conductivity of silicon. Here, the base temperature is obtained by substituting the conduction temperature drop through the silicon substrate; the values of wall temperature difference are shown in Fig. S4 in the Supplementary Information.

The CuIO-MMC exhibited a heat transfer coefficient of 39.2–147 kW m^{-2} K^{-1} while dissipating a heat flux range of 100–1150 W cm^{-2} with a fin efficiency of 0.93–0.98. In particular, the heat transfer coefficient is in the range of h_{eff} = 55.5–93.4 kW m^{-2} K^{-1} for a channel width of 50 μm as shown in Fig. 4(c). By comparison, for a channel width of 200 μm, the heat transfer coefficient increased by 26.7 %–37.1 % owing to the larger wetting area and an increase in the overall fluid velocity, resulting in h_{eff}

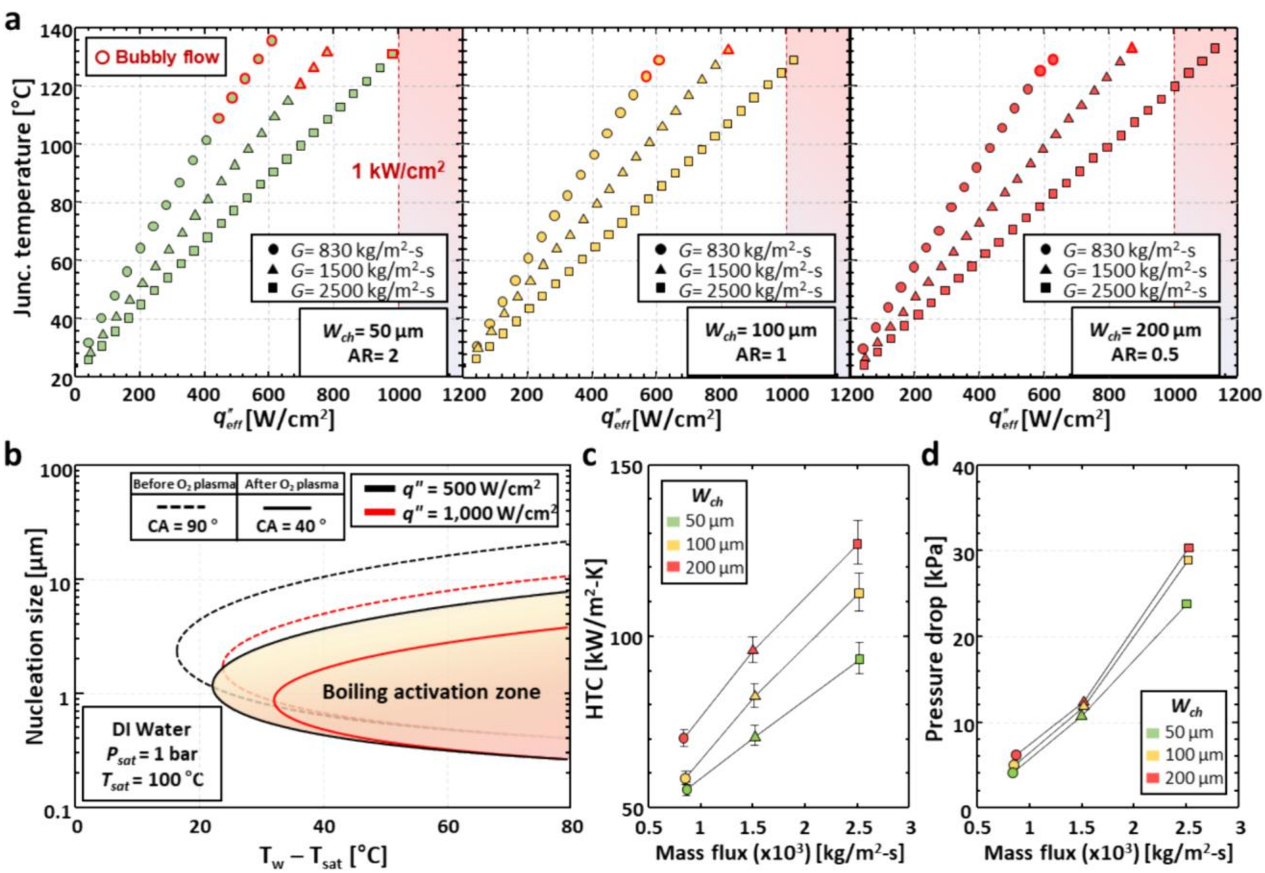

Fig. 4. Thermofluidic performance of the CuIOs-MMC cooler. Characterization of (a) junction temperature. Red outlines indicate the bubbly flow boiling regime. (b) Prediction of wall superheat temperature and pore sizes with decreasing CA. (c) Averaged convective heat transfer coefficient and (d) pressure drop through the microcooler as a function of mass flux at a uniform heat flux $q'' = 500$ W cm^{-2}. (For interpretation of the references to colour in this figure legend, the reader is referred to the web version of this article.)

$= 70.4$–127.1 kW m^{-2} K^{-1}. In addition, the thermal conductivity of water increased with increasing fluid temperature, which resulted in a continuous increase in the heat transfer coefficient with increasing heat flux. In the CuIO-MMC with $W_{ch} = 50$ μm, $q'' = 610$–982 W cm^{-2} was removed despite the low flow rate (34–100 g min^{-1}), and the CuIO-MMC with $W_{ch} = 200$ μm showed the ability to dissipate $q'' = 627$–1147 W cm^{-2} using a relatively high flow rate (64–192 g min^{-1}). The subcooled boiling could be promoted at a higher surface temperature than $T_h = \sim120$ °C with the aid of the microporous structures of CuIOs, which have the advantage of increasing the heat transfer rate owing to the nucleate boiling at high heat fluxes over $q'' = 1500$ W cm^{-2}.

The pressure drop during heat removal from the CuIOs-MMC is shown in Fig. 4(d). Overall, the CuIOs-MMC maintained a low pressure drop of 4–32 kPa despite the high mass flux from the small hydraulic diameter, thanks to the formation of a very short flow path inside the microchannel (i.e., $L_{ch} = W_{MF,wall} + (W_{MF,in} + W_{MF,out}) / 2$). In our study, L_{ch} was fixed at 1.3 mm, which was four times shorter than the full channel length of 5 mm. Notably, the high mass flux (G=2500 kg m^{-2} s^{-1}) in the CuIOs-MMC with $W_{ch} = 200$ μm exhibited a low pressure drop of 24–25 kPa, even with the highest mass flow rate of $\dot{m} = 190$ g min^{-1}. This configuration achieved the lowest total thermal resistance, indicating that it could support a high heat-flux dissipation, thereby providing a large in-chip thermal budget. Moreover, the viscosity of the fluid itself decreased as the heat flux increased, and therefore a 5 %–13 % decrease in the total pressure drop occurred compared to the non-heating condition. The boiling incipience occurred at a heat flux higher than 600 W cm^{-2}; however, the bubble condensed and shrank immediately because of a relatively large subcooled temperature ($\Delta T_{sub} = 82$–85 K) and thus led to only a small increase of ~ 1 kPa in the pressure drop (see Fig. S5 in Supplementary Information). Additional information on the dimensionless analysis of the Nusselt number and the friction factor regarding current hydraulic–thermal performance can be found in Fig. S6 and Fig. S7.

3.3. Thermal resistances on CuIO-MMC

Here, we analyze the detailed thermal–hydraulic performance of CuIOs-MMC in terms of pumping power and thermal resistance based on the results of temperature and pressure drop. The enhancement of single-phase heat transfer in CuIOs-MMC primarily occurs because of the vertical flow from the distributed liquid at the manifold to the microchannel. During this process, the impinging jet effect on the channel bottom and the mixing effect create a thin thermal boundary layer, thereby reducing the junction temperature (Fig. S8). Additionally, the large surface area with a high porosity of $\varepsilon = 0.75$–0.85 [50] and high effective thermal conductivity of $k_{eff,\ CuIO}$=80 W m^{-1} K^{-1} [51] further aids in the effective dissipation of heat flux. At high heat fluxes, the CuIOs facilitate nucleate boiling more effectively compared to smooth surfaces, enhancing the heat transfer coefficient by improved two-phase flow boiling. Furthermore, the short flow path of the MMC through the microchannel helps mitigate two-phase instability and safely removes high heat flux. Fig. 5(a) presents a comparison of junction temperature between bare MMC [31] and CuIOs-MMC at a mass flow rate of ~ 200 g min^{-1}. Although the bare MMC had a denser manifold and microchannel configuration than CuIO-MMC, the junction temperature of CuIOs-MMC was lower than that of bare MMC. In particular, the junction temperature of CuIOs-MMC was 8.9 °C less than that of bare MMC at a heat flux of 1000 W cm^{-1} by additionally expanding the copper

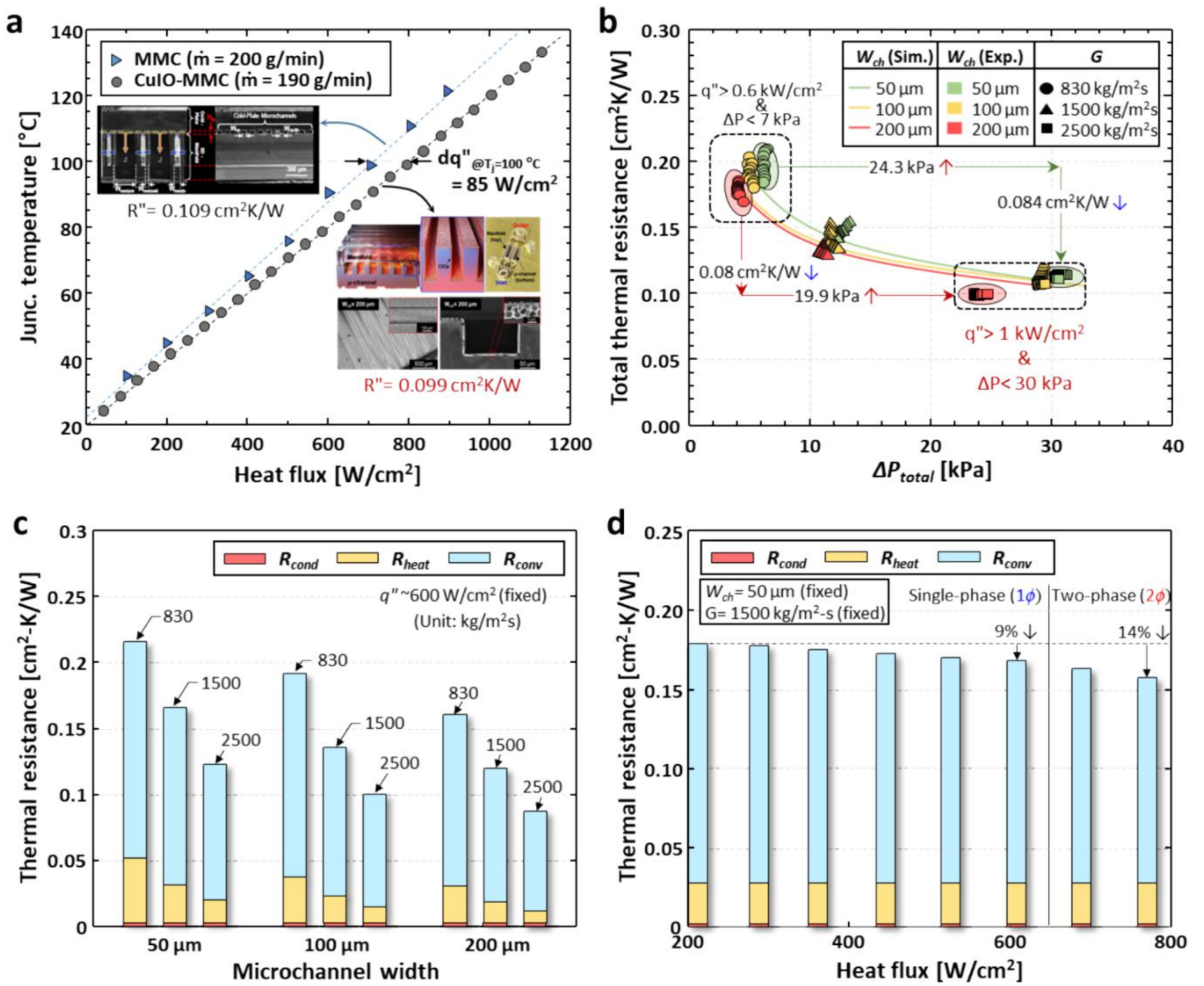

Fig. 5. Analysis of the thermal resistance of CuIOs-MMC. (a) Comparison of junction temperature between bare MMC and CuIOs-MMC. (b) Total thermal resistance as a function of total pressure drop on CuIOs-MMC. The solid line indicates the simulation results at $q'' = 400$ W cm^{-2}, showing good agreement with experimental data. (c) Detailed proportion of total thermal resistance on the different channel widths at the fixed heat flux of $q'' = \sim 600$ W cm^{-2}. (d) Distribution of thermal resistance for different heat fluxes over a given channel width of $W_{ch} = 50$ μm.

surface area. Furthermore, the total thermal resistance, calculated from the temperature difference between the average heated-surface temperature and inlet fluid temperature and the given heat flux (i.e., $R_{tot} = (T_h - T_{f,in}) / q''$), was reduced by 0.01 cm^2 K W^{-1} on CuIOs-MMC. This reduction in thermal resistance on CuIOs-MMC demonstrates that the implementation of CuIO in the microchannel can enhance the thermal performance by 8.1 % compared to bare MMC.

Summarizing the thermal and hydraulic performance of CuIOs-MMCs under different geometrical and flow rate variations, we present the total thermal resistance as a function of the pressure drop in Fig. 5(b). Depending on the three widths of the microchannel, the total thermal resistance varied between 0.1 and 0.2 cm^2 K W^{-1} and the pressure drop ranged from 4 to 32 kPa. When the aspect ratio of the microchannel width decreased from 2 to 0.5, along with an increase in channel width from 50 to 200 μm, there was a substantial reduction in pressure drop by 4.7 %–17.9 %. Moreover, the CuIOs-MMCs showed a decrease in total thermal resistance by 3.4 %–12.0 % with a smaller aspect ratio, in contrast to conventional microchannels that exhibit better thermal performance in high-aspect-ratio channels [52]. This improvement of heat transfer in CuIOs-MMCs with a small aspect ratio primarily resulted from the impinged water jet to the bottom surface of channel base and the developing flow near the microchannel inlet. The changes in the manifold-to-microchannel area in the short path create the developing region, which generates the mixing regime and a thin thermal boundary layer and improves the wall heat transfer efficiency [29]. Moreover, the full-scale conjugate simulation results for all three microcoolers exhibited good agreement with experimental data, which indicated that the mean absolute error (MAE) of total thermal resistance and pressure drop for all three geometries was $MAE_{Rtot} = 3.12$ % and $MAE_{\Delta P}$=11.3 % at the same heat flux of $q'' = 400$ W cm^{-2} (see Fig. S9 in the Supplementary Information).

To explore the contribution to thermal resistance, the total thermal resistance was divided into three components: the portion of conduction through the substrate (R_{cond}), convective heat transfer (R_{conv}), and heating thermal resistance (R_{heat}). Fig. 5(c) and (d) illustrate a detailed breakdown of each thermal resistance, while the definitions of each thermal resistance can be found in Fig. S10. An analysis of R_{tot} in Fig. 5 (c) indicates that the convective thermal resistance accounts for the largest portion, comprising up to 83.5 % of the total thermal resistance, and heating and conduction thermal resistance account for 15.4 % and 1.1 %, respectively. Among them, R_{heat} and R_{conv} can possibly be reduced by increasing the inlet temperature and vigorously boiling at a higher heat flux, respectively. Furthermore, as the channel widths increase, the substantially higher flow rate promotes the enforcement of convective heat transfer, while the heated fluid temperature decreases under the energy balance. Under the effect of heat flux, as shown in Fig. 5(d), heating thermal resistance showed an almost constant value because the fluid temperature proportionally increased with the heat flux. Meanwhile, convective thermal resistance gradually decreased by 9 % compared to the initial heating condition with the help of the increased thermal conductivity of water and velocity due to the decrease in viscosity in the channels. Convective thermal resistance in two-phase conditions decreased by 5 % more in addition to the effect of thermophysical properties in the single phase. Flow boiling in CuIO-MMC cannot be well activated owing to the junction temperature limit of 130 °C; however, we observed great potential to utilize the two-phase cooling to dissipate ultrahigh heat fluxes over 1500 W cm^{-2}.

3.4. Temperature uniformity

MMCs have great potential for improving the thermal uniformity of the chip temperature in addition to enhancing the heat transfer rate. Fig. 6(a) shows infrared (IR) thermal images depicting the temperature distribution on the heated surface, while Fig. 6(b) and (c) illustrate the temperature variations in parallel and vertical directions with respect to the manifold flow direction, respectively. Here, the wavy temperature lines are a trend created during passage through the line of a serpentine heater with a length and width of 300 and 200 μm, respectively, which mimics actual device heat-dissipation behaviors. The CuIOs-MMC substantially reduced temperature nonuniformity along the flow direction (x-axial direction) with the aid of an impinging jet by the manifold inlet channel. Otherwise, a relatively large thermal gradient occurred along the y-axis direction, particularly in the vicinity of the outlet conduit manifolds. This could be attributed to the increased sensible heat of the fluid and the relatively low heat-transfer coefficients caused by the lower fluid velocity in the microchannels beneath the outlet manifolds due to their larger width than the inlet manifold width.

To observe the thermal uniformity quantitively, the temperature uniformity (ΔT_u) of the CIOs-MMC was calculated from the local surface temperature extracted from the IR images. ΔT_u was calculated from the local temperature corresponding to each pixel of IR images as follows:

$$\Delta T_u = \sqrt{\frac{1}{n}\sum_{i=1}^{n}\left(T_{lc,i} - T_{avg}\right)^2} \quad (8)$$

An example of the temperature uniformity results for the CuIO-MMC with a channel width of 50 μm is shown in Fig. 6(d). Excellent temperature uniformity was achieved by CuIOs-MMC, with a maximum temperature deviation of less than 6 °C over the junction temperature of 5 × 5 mm^2 while dissipating extreme heat fluxes up to 1000 W cm^{-2}. The higher mass flux of G=2,500 kg m^{-2} s^{-1} exhibited a lower temperature deviation ranging from 1.3 °C to 3.3 °C at the heat flux of $q'' =$ 250–600 W cm^{-2} compared to 2.3 °C-5.4 °C for the mass flux of G=830 kg m^{-2} s^{-1} owing to the increase in convective heat transfer. Although we only conducted the test with a single manifold structure, increasing the number of inlet and outlet conduits could possibly lead to additional improvements in thermal uniformity because the temperature variation along the y-axis can be minimized by reducing the outlet manifold width.

3.5. Benchmarking of thermal performances with other embedded MMCs

An extensive comparison of thermal–hydraulic performance has been presented between CuIOs-MMC and other embedded MMCs in the literature. Fig. 7(a) depicts the maximum dissipated heat fluxes versus the heated area of the chip. The group that utilized DI water [26,32,37,38,53–56] as a coolant demonstrated a wide capability of heat removal up to $q'' = 1.7$ kW cm^{-2}. A few studies using dielectric liquids such as HFE-7100 [33–35] and R-245fa [36] reported the removal of high heat fluxes in the range of $q'' = 0.5$–0.9 kW cm^{-2} by utilizing two-phase cooling. Clearly, the development of the thermal boundary layer decreases as the size of the chip gradually decreases when using liquid cooling. Consequently, there is an exponential increase in the maximum heat flux that can be dissipated. The CuIOs-MMC configuration achieved a peak heat flux of $q'' = 1.2$ kW cm^{-2} on a 5 × 5 mm^2 unit heater, marking a record value. Reported hydraulic–thermal data of CuIOs-MMC demonstrate enhanced thermal performance, which is facilitated by engineered CuIO surfaces, enabling effective heat-flux removal. This highlights the potential for leveraging manifold structures and CuIOs on embedded chips to efficiently cool large-area electronic devices. This approach enhances heat transfer and ensures

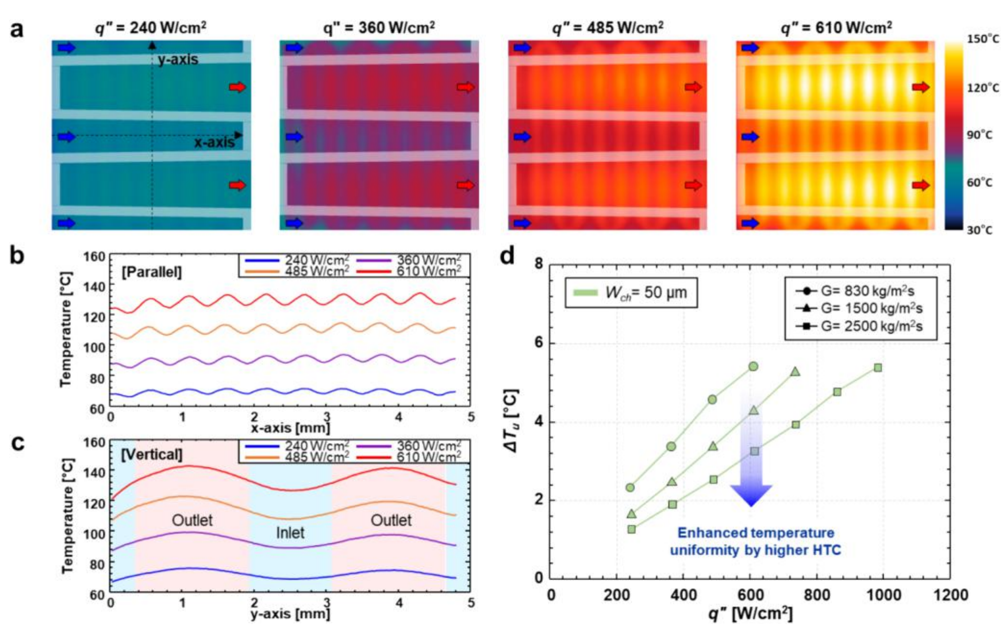

Fig. 6. Temperature uniformity over the heated area. (a) Temperature distribution of the heat source recorded by an IR camera and the exported thermal gradients with (b) parallel and (c) vertical lines. (d) Temperature deviation of the entire heated area in CuIOs-MMC with $W_{ch} = 50$ μm.

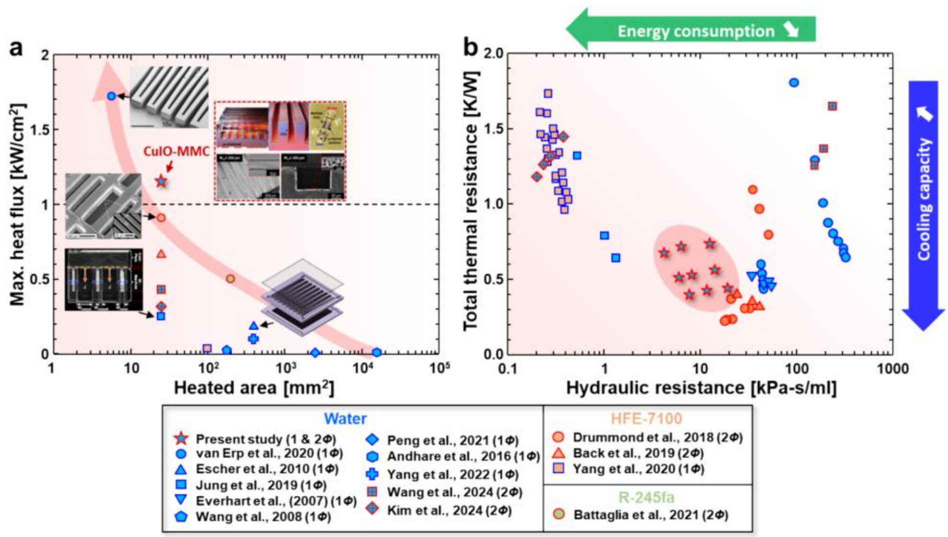

Fig. 7. Benchmarking of thermal–hydraulic performance with other embedded MMCs. (a) Effect of heater size on the maximum dissipated heat flux and (b) total thermal resistance of MMCs using direct cooling as a function of pressure drop per unit volumetric flow rate.

superior thermal uniformity, thereby mitigating heat flux degradation.

The other benchmark is a comparison with the minimum total thermal resistance at the removed highest heat flux and the applied hydraulic resistance (R_H) as shown in Fig. 7(b). According to this benchmark, hydraulic resistance is defined as the total pressure drop per volumetric flow rate. The group that used DI water demonstrated a comparable thermal resistance of R_{tot} = 0.4–0.65 W K^{-1}, even though it was used for single-phase cooling, owing to the superior thermophysical properties of water over dielectric liquids. Hydraulic resistance showed a wide range of R_H=1–300 kPa s ml^{-1} depending on the design of manifold configuration and hydraulic channel diameter. By contrast, MMCs using HFE-7100 facilitated lower R_{tot} = 0.2–0.3 W K^{-1} at a high heat flux of q'' = 660–910 W cm^{-2} owing to active two-phase cooling. However, even if they achieved the lowest thermal resistance using two-phase cooling, the substantially increased hydraulic resistance of R_H=20–50 kPa s ml^{-1} from flow boiling with a high exit quality of 0.1–0.3 was required to remove the high heat flux. The remarkable results of the present study show that the lowest total thermal resistance of R_{tot} = 0.4–0.45 W K^{-1} was achieved among the MMCs using DI water while generating minimum hydraulic resistance under 10 kPa s ml^{-1} with the help of an optimized manifold configuration and the CuIO structure. A comprehensive analysis of hydraulic–thermal performance using the coefficient of performance can be found in Fig. S11 in Supplementary Information. Therefore, The CuIOs-MMC removes extremely high heat fluxes of q'' = 1.15 kW cm^{-2} while retaining a very low pressure drop of ΔP<32 kPa, thus guaranteeing significantly higher energy efficiency compared to benchmark works.

4. Conclusions

In this study, we developed a CuIO structure in manifold microchannel coolers and performed experimental microfluidic tests on the coolers for an embedded cooling system used in high-power electronics. This innovative approach demonstrates that a high heat flux of q'' = 1147 W cm^{-2} can be removed at a wall temperature difference of ΔT_{wall} = 60 K by utilizing CuIOs, which expand the heat transfer area and facilitate nucleate boiling. It also shows that the pressure drop applied inside the cooler can be kept lower than ΔP=32 kPa owing to the integration with the manifold liquid route and the shortening of the flow path inside the microchannels, resulting in the lowest convective thermal resistance of R_{conv} = 0.068 cm^2 K W^{-1} with a low hydraulic resistance of R_H<10 kPa s ml^{-1}. In the future, further investigations into the effect of surface roughness and two-phase phenomena in MMCs using dielectric liquids are required to meet practical and reliable interchip cooling requirements. In conclusion, we present a disruptive thermal-management solution that significantly enhances the cooling efficiency of high-performance electronics using a manifold microchannel with CuIOs and provide a potential breakthrough for electronic devices subjected to extreme heat flux, such as defense weapons, data centers, and electric vehicle power electronics.

CRediT authorship contribution statement

Daeyoung Kong: Writing – original draft, Methodology, Formal analysis, Data curation, Conceptualization. **Heungdong Kwon:** Methodology, Investigation. **Bongho Jang:** Methodology, Investigation. **Hyuk-Jun Kwon:** Supervision, Methodology. **Mehdi Asheghi:** Writing – review & editing, Supervision. **Kenneth E. Goodson:** Writing – review & editing, Supervision. **Hyoungsoon Lee:** Writing – review & editing, Project administration, Funding acquisition.

Declaration of competing interest

The authors declare that they have no known competing financial interests or personal relationships that could have appeared to influence the work reported in this paper.

Data availability

Data will be made available on request.

Acknowledgments

This research was supported by the Challengeable Future Defense Technology Research and Development Program through the Agency for Defense Development (ADD) funded by the Defense Acquisition Program Administration in 2021 (No.915028201).

Appendix A. Supplementary data

Supplementary data to this article can be found online at https://doi.org/10.1016/j.enconman.2024.118809.

References

[1] Sohel Murshed SM, Nieto de Castro CA. A critical review of traditional and emerging techniques and fluids for electronics cooling. Renew Sustain Energy Rev 2017;78:821–33.
[2] Pengelly RS, Wood SM, Milligan JW, Sheppard ST, Pribble WL. A Review of GaN on SiC High Electron-Mobility Power Transistors and MMICs. IEEE Trans Microwave Theory Techn 2012;60:1764–83.
[3] Bar-Cohen A, Asheghi M, Chainer T, Garimella SV, Goodson K, Gorle C, et al. The ICECool Fundamentals Effort on Evaporative Cooling of Microelectronics. IEEE Trans Compon, Packag Manufact Technol 2021:1.
[4] Li Z, Luo H, Jiang Y, Liu H, Xu L, Cao K, et al. Comprehensive review and future prospects on chip-scale thermal management: Core of data center's thermal management. Appl Therm Eng 2024;251:123612.
[5] van Erp RFP. Near-junction microfluidic cooling for high power-density GaNon-Si electronics: A wafer, device, packaging, and system-level investigation. EPFL, Lausanne: PhD; 2022.
[6] Tuckerman DB, Pease RFW. High-performance heat sinking for VLSI. IEEE Electron Device Lett 1981;2:126–9.
[7] Woodcock C, Yu X, Plawsky J, Peles Y. Piranha Pin Fin (PPF) — Advanced flow boiling microstructures with low surface tension dielectric fluids. Int J Heat Mass Transf 2015;90:591–604.
[8] Kong D, Jung KW, Jung S, Jung D, Schaadt J, Iyengar M, et al. Single-phase thermal and hydraulic performance of embedded silicon micro-pin fin heat sinks using R245fa. Int J Heat Mass Transf 2019;141:145–55.
[9] Guye K, Dong D, Kim Y, Lee H, Dogruoz B, Agonafer D. Guidelines for Designing Micropillar Structures for Enhanced Evaporative Heat Transfer. J Electron Packag 2021;143:041106.
[10] Feng S, Yan Y, Li H, Xu F, Zhang L. Heat transfer characteristics investigations on liquid-cooled integrated micro pin-fin chip with gradient distribution arrays and double heating input for intra-chip micro-fluidic cooling. Int J Heat Mass Transf 2020;159:120118.
[11] C. Woodcock, C. Ng'oma, M. Sweet, Y. Wang, Y. Peles, J. Plawsky, Ultra-high heat flux dissipation with Piranha Pin Fins, *Int. J. Heat Mass Transf.* 128 (2019) 504–515.
[12] Han Y, Lau BL, Zhang X. Package-Level Microjet-Based Hotspot Cooling Solution for Microelectronic Devices. IEEE Electron Device Lett 2015;36:502–4.
[13] Shin J-H, Rozenfeld T, Shockner T, Vutha AK, Wang Y, Ziskind G, et al. Local heat transfer under an array of micro jet impingement using HFE-7000. Appl Thermal Eng 2019:16.
[14] Ndao S, Peles Y, Jensen MK. Effects of pin fin shape and configuration on the single-phase heat transfer characteristics of jet impingement on micro pin fins. Int J Heat Mass Transf 2014;70:856–63.
[15] Liang G, Mudawar I. Review of spray cooling – Part 1: Single-phase and nucleate boiling regimes, and critical heat flux. Int J Heat Mass Transf 2017;115:1174–205.
[16] Kim Y, Jung S, Kim S, Choi ST, Kim M, Lee H. Heat transfer performance of water-based electrospray cooling. Int Commun Heat Mass Transf 2020;118:104861.
[17] D.H. Altman, A. Gupta, M. Tyhach, Development of a Diamond Microfluidics-Based Intra-Chip Cooling Technology for GaN, in: Volume 3: Advanced Fabrication and Manufacturing; Emerging Technology Frontiers; Energy, Health and Water-Applications of Nano-, Micro- and Mini-Scale Devices; MEMS and NEMS; Technology Update Talks; Thermal Management Using Micro Channels, Jets, Sprays, American Society of Mechanical Engineers, San Francisco, California, USA, 2015: p. V003T04A006.
[18] Han Y, Lau BL, Tang G, Zhang X. Thermal Management of Hotspots Using Diamond Heat Spreader on Si Microcooler for GaN Devices. IEEE Trans Compon Packag Manufact Technol 2015;5:1740–6.
[19] Khan SA, Koç M, Al-Ghamdi SG. Urban concentrated photovoltaics: Advanced thermal management system using nanofluid and microporous surface. Energy Convers Manag 2020;222:113244.
[20] Qi C, Luo T, Liu M, Fan F, Yan Y. Experimental study on the flow and heat transfer characteristics of nanofluids in double-tube heat exchangers based on thermal efficiency assessment. Energy Convers Manag 2019;197:111877.
[21] Hajatzadeh Pordanjani A, Aghakhani S, Afrand M, Mahmoudi B, Mahian O, Wongwises S. An updated review on application of nanofluids in heat exchangers for saving energy. Energy Convers Manag 2019;198:111886.
[22] Leong KC, Ho JY, Wong KK. A critical review of pool and flow boiling heat transfer of dielectric fluids on enhanced surfaces. Appl Therm Eng 2017;112:999–1019.
[23] Liang G, Mudawar I. Review of channel flow boiling enhancement by surface modification, and instability suppression schemes. Int J Heat Mass Transf 2020; 146:118864.
[24] Kong D, Kim Y, Kang M, Song E, Hong Y, Kim HS, et al. A holistic approach to thermal-hydraulic design of 3D manifold microchannel heat sinks for energy-efficient cooling. Case Stud Therm Eng 2021;28:101583.
[25] Tang J, Li X, Hu R, Mo Z, Du M. A novel designed manifold ultrathin micro pin-fin channel for thermal management of high-concentrator photovoltaic system. Int J Heat Mass Transf 2022;183:122094.
[26] Jung KW, Kharangate CR, Lee H, Palko J, Zhou F, Asheghi M, et al. Embedded cooling with 3D manifold for vehicle power electronics application: Single-phase thermal-fluid performance. Int J Heat Mass Transf 2019;130:1108–19.
[27] Ye Y, Zhang N, Yu L, Cong B, Liu R, Kong Y, et al. In: Integrated Electrical Test Vehicle Co-designed with Microfluidics for Evaluating the Performance of Embedded Cooling. Xiamen, China: IEEE; 2021. p. 21–5.
[28] Kong D, Jung E, Kim Y, Manepalli VV, Rah KJ, Kim HS, et al. An additively manufactured manifold-microchannel heat sink for high-heat flux cooling. Int J Mech Sci 2023;108228.
[29] Wang Y, Ding G-F. Experimental investigation of heat transfer performance for a novel microchannel heat sink. J Micromech Microeng 2008;18:035021.
[30] Escher W, Brunschwiler T, Michel B, Poulikakos D. Experimental Investigation of an Ultrathin Manifold Microchannel Heat Sink for Liquid-Cooled Chips. J Heat Transf 2010;132.
[31] Jung KW. Investigation thermo-fluidic performance of si-based embedded microchannels-3d manifold cooling system for high power density electronic applications. Stanford University; 2020. Ph.D. thesis,.
[32] van Erp R, Soleimanzadeh R, Nela L, Kampitsis G, Matioli E. Co-designing electronics with microfluidics for more sustainable cooling. Nature 2020;585: 211–6.
[33] Drummond KP, Back D, Sinanis MD, Janes DB, Peroulis D, Weibel JA, et al. A hierarchical manifold microchannel heat sink array for high-heat-flux two-phase cooling of electronics. Int J Heat Mass Transf 2018;117:319–30.
[34] Back D, Drummond KP, Sinanis MD, Weibel JA, Garimella SV, Peroulis D, et al. Design, Fabrication, and Characterization of a Compact Hierarchical Manifold Microchannel Heat Sink Array for Two-Phase Cooling. IEEE Trans Compon Packag Manufact Technol 2019;9:1291–300.
[35] Yang M, Li M-T, Hua Y-C, Wang W, Cao B-Y. Experimental study on single-phase hybrid microchannel cooling using HFE-7100 for liquid-cooled chips. Int J Heat Mass Transf 2020;160:120230.
[36] Battaglia F, Singer F, Deisenroth DC, Ohadi MM. Experimental Characterization of Two-Phase Cooling of Power Electronics in Thermosiphon and Forced Convection Modes. J Electron Packag 2021;143:031006.
[37] Wang S, Chen H-H, Chen C-L. Enhanced flow boiling in silicon nanowire-coated manifold microchannels. Appl Therm Eng 2019;148:1043–57.
[38] Kim K, Kong D, Kim Y, Jang B, Cho J, Kwon H-J, et al. Enhanced boiling heat transfer via microporous copper surface integration in a manifold microgap. Appl Therm Eng 2024;241:122325.
[39] Sun B, Li J. Toward extremely low thermal resistance with extremely low pumping power consumption for ultra-high heat flux removal on chip size scale. Energy Convers Manag 2024;306:118293.
[40] Kwon H, Wu Q, Kong D, Hazra S, Jiang K, Narumanchi S, et al. Capillary-enhanced two-phase micro-cooler using copper-inverse-opal wick with silicon microchannel manifold for high-heat-flux cooling application. Int Commun Heat Mass Transf 2024;156:107592.
[41] Zhang C, Palko JW, Barako MT, Asheghi M, Santiago JG, Goodson KE. Enhanced Capillary-Fed Boiling in Copper Inverse Opals via Template Sintering. Adv Funct Mater 2018;28:1803689.
[42] Palko JW, Lee H, Zhang C, Dusseault TJ, Maitra T, Won Y, et al. Extreme Two-Phase Cooling from Laser-Etched Diamond and Conformal, Template-Fabricated Microporous Copper. Adv Funct Mater 2017;27:1703265.
[43] Gajasinghe RWRL, Senveli SU, Rawal S, Williams A, Zheng A, Datar RH, et al. Experimental study of PDMS bonding to various substrates for monolithic microfluidic applications. J Micromech Microeng 2014;24:075010.
[44] Chaudhary A, Barshilia HC. Nanometric Multiscale Rough CuO/Cu(OH) 2 Superhydrophobic Surfaces Prepared by a Facile One-Step Solution-Immersion Process: Transition to Superhydrophilicity with Oxygen Plasma Treatment. J Phys Chem C 2011;115:18213–20.
[45] McDonald BT, Cui T. Superhydrophilic surface modification of copper surfaces by Layer-by-Layer self-assembly and Liquid Phase Deposition of TiO2 thin film. J Colloid Interface Sci 2011;354:1–6.
[46] Galvan Y, Phillips KR, Haumann M, Wasserscheid P, Zarraga R, Vogel N. Ionic-Liquid-Infused Nanostructures as Repellent Surfaces. Langmuir 2018;34:6894–902.
[47] Owen MJ, Smith PJ. Plasma treatment of polydimethylsiloxane. J Adhes Sci Technol 1994;8:1063–75.
[48] Barreca D, Gasparotto A, Tondello E. CVD Cu2O and CuO Nanosystems Characterized by XPS. Surf Sci Spectra 2007;14:41–51.
[49] Liu D, Lee P-S, Garimella SV. Prediction of the onset of nucleate boiling in microchannel flow. Int J Heat Mass Transf 2005;48:5134–49.
[50] Kong D, Kim K, Jung E, Jiang K, Wu Q, Jang B, et al. Boiling-induced thermal degradation of copper inverse opals and its mitigation. Int Commun Heat Mass Transf 2024;151:107250.
[51] Barako MT, Weisse JM, Roy S, Kodama T, Dusseault TJ, Motoyama M, et al. Thermal conduction in nanoporous copper inverse opal films. In: Fourteenth Intersociety Conference on Thermal and Thermomechanical Phenomena in Electronic Systems (ITherm). Orlando, FL, USA: IEEE; 2014. p. 736–43.
[52] Pan Y-H, Zhao R, Fan X-H, Nian Y-L, Cheng W-L. Study on the effect of varying channel aspect ratio on heat transfer performance of manifold microchannel heat sink. Int J Heat Mass Transf 2020;163:120461.
[53] L. Everhart, N. Jankowski, B. Geil, A. Bayba, D. Ibitayo, P. McCluskey, Manifold Microchannel Cooler for Direct Backside Liquid Cooling of SiC Power Devices, in: ASME 5th International Conference on Nanochannels, Microchannels, and Minichannels, ASMEDC, Puebla, Mexico, 2007: pp. 285–292.
[54] Andhare RS, Shooshtari A, Dessiatoun SV, Ohadi MM. Heat transfer and pressure drop characteristics of a flat plate manifold microchannel heat exchanger in counter flow configuration. Appl Therm Eng 2016;96:178–89.
[55] Peng Y, Li Z, Li S, Cao B, Wu X, Zhao X. The experimental study of the heat ransfer performance of a zigzag-serpentine microchannel heat sink. Int J Therm Sci 2021; 163:106831.
[56] Yang Y, Du J, Li M, Li W, Wang Q, Wen B, et al. Embedded microfluidic cooling with compact double H type manifold microchannels for large-area high-power chips. Int J Heat Mass Transf 2022;197:123340.